nature astronomy

SUPPLEMENTARY INFORMATION

https://doi.org/10.1038/s41550-019-0806-z

In the format provided by the authors and unedited.

Trans-Neptunian binaries as evidence for planetesimal formation by the streaming instability

David Nesvorný[1*], Rixin Li[2], Andrew N. Youdin[2], Jacob B. Simon[1,3] and William M. Grundy[4]

[1]Department of Space Studies, Southwest Research Institute, Boulder, CO, USA. [2]Steward Observatory & Department of Astronomy, University of Arizona, Tucson, AZ, USA. [3]JILA, University of Colorado, Boulder, CO, USA. [4]Lowell Observatory, Flagstaff, AZ, USA. *e-mail: davidn@boulder.swri.edu

Supplementary Information for Trans-Neptunian Binary Evidence for Planetesimal Formation by the Streaming Instability

David Nesvorný, Rixin Li, Andrew N. Youdin, Jacob B. Simon, William M. Grundy

1. Observations of trans-Neptunian binaries

Trans-Neptunian binaries (TNBs) with known orbits are tabulated in ref. [6] and also in Supplementary Table 1. Using the Hubble Space Telescope and laser guide star adaptive optics on large ground-based telescopes, multi-epoch images of each TNB system were obtained at spatial resolutions sufficiently high to separate the primary and secondary bodies. Relative positions of the two bodies were measured via PSF-fitting techniques, and Keplerian orbits were fitted to the relative astrometry data. Uncertainties in the fitted orbital elements were determined via the bootstrap Monte Carlo method. Repeatedly randomizing the astrometric observations consistent with their uncertainties and re-fitting the Keplerian elements produced a cloud of orbit solutions representative of the probability distribution of orbital solutions. The ambiguity between the true orbit and its mirror through the sky plane has been broken for the majority of the systems, thanks to the accumulation of parallax from the relative motions of Earth and the TNB around the Sun.

Relative to earlier work on measuring the orbital distribution of TNBs, ref. [6] has a much larger sample of fully-determined binary orbits, 34 in total (Supplementary Table 1). For comparison, ref. [50] only had 9 fully-determined binary orbits (7 prograde, 2 retrograde). The much larger size of the new dataset allows us, for the first time, to perform a detailed comparison between model and observations.

2. Dependence of clump obliquities on various parameters

In Figure 3 of the main text we show the distribution of clump obliquities for time $t_{\rm sg} = 4/\Omega$ in run A12. Here we discuss how the distribution of obliquities varies (1) in different simulations, (2) with time, and (3) how it depends on the clump mass.

As for (1), the obliquity distribution of clumps is similar in all our runs (Supplementary Figure 1). The preference for prograde binary orbits is 75-80%. The run C203, which shows a slightly shallower distribution, is also the run where fewer clumps formed. The distribution for run C203 may thus be affected by insufficient statistics.

As for (2), the obliquity distribution becomes slightly broader over time (Supplementary Figure 2). This happens, at least in part, because the individual clumps in our `ATHENA` simulations remain spatially extended. The gravitational interaction of (artificially) extended clumps (see Figure 1 and Supplementary Video) then acts to gradually randomize the obliquity distribution. In reality, the clumps must collapse into binary planetesimals which are expected to preserve the initial rotation. For this reason, the situation for $t_{\rm sg} = 4/\Omega$ in run A12 (Figure 3 in the main text) best represents our expectation for the obliquity distribution from the SI. The behavior in other runs is similar.

As for (3), Supplementary Figure 3 shows the dependence of the obliquity distribution on the clump mass. The more massive clumps show a stronger preference for prograde rotation than the less massive clumps. The reasons behind this trend are presently unclear. It is also not possible to establish whether the same trend exists in the observational data, because the CC binaries have similar masses and the existing statistic is not good enough to resolve modest dependencies such as the one shown in Supplementary Figure 3.

We also investigated the relationship between the vorticity of the particle field, as defined in the main text, and clump rotation (Supplementary Figure 4). Specifically, we determined the colatitude distribution of the vorticity vectors before and after the self-gravity was switched on. The colatitude distribution is initially broad and shows a slight preference for retrograde rotation (see $t_{\rm sg} = 0$ in the left panel of Supplementary Figure 4). This is a consequence of the SI-induced vertical motion of particles. After the gravity is switched on (see $t_{\rm sg} > 0$ in the right panel of Supplementary Figure 4), the colatitude distribution becomes similar to the distribution of clump obliquities.

3. Planetesimal mass

As noted in the methods section, our local planetesimal formation simulations have several key input parameters, including $\tilde{G}$ for the strength of self-gravity and Π for the strength of radial pressure gradients driving particle drift and SI. The mass of planetesimals (i.e. bound protoplanetesimal clumps) is measured in the code unit, $M_{\rm local} = \rho_0 H^3$, where ρ_0 is the midplane gas density and H is the gas-scale height.

Additional assumptions about the disk model are needed to translate to physical mass units, even after we have specified the disk location (near 45 AU) and the simulation input parameters. The four relevant properties of the global disk model are the local temperature, T, and gas surface density $\Sigma_{\rm g}$ and the local powerlaw slopes of these two quantities. Here we describe physical disk models consistent with our simulations, which allow us to assign physical masses to our planetesimal formation simulations.

A useful disk property is the aspect ratio

$$h = H/r = 0.067\sqrt{T_{25}R_{45}} \tag{1}$$

which mainly depends on temperature, here scaled as $T_{25} = T/(25\,\mathrm{K})$. We have also scaled $R_{45} = r/(45\,\mathrm{AU})$, and a Solar mass star and mean molecular weight of 2.34 have been assumed. Our fiducial temperature is cooler than a fully flared disk model would predict, i.e. $T = 39R_{45}^{-3/7}$ K [51]. Our cooler temperatures are possible if dust sediments, and the disk surface intercepts less stellar flux. Though a perfect flat disk might be as cold as $T = 5R_{45}^{-3/4}$ K (approaching the CMB!), temperatures are likely higher than this limit, due to heating from the ambient dust envelope and/or the interstellar radiation field [52,53].

We can express the code mass as

$$M_{\rm local} = \rho_0 H^3 = h^3 \tilde{G}\frac{M_*}{4\pi} \tag{2}$$

$$\simeq 2500(T_{25}R_{45})^{3/2}\frac{\tilde{G}}{0.05}\, M_{\rm Cer} \tag{3}$$

with $M_{\rm Cer} = 9.4 \times 10^{23}$ g.

Our simulations produce maximum clump masses of $\simeq 10^{-4} M_{\rm local}$ (runs A and C) and $\simeq 3 \times 10^{-4} M_{\rm local}$ (run B). Using the above scalings, our simulations (which indeed set $\tilde{G} = 0.05$) produce maximum masses of $\simeq$(0.25-0.75) $T_{25}^{3/2}\, M_{\rm Cer}$. The maximum mass of CCs is $\sim 0.015 M_{\rm Cer}$ (estimated for the maximum radius of $\simeq$150 km and density 1 g cm^{-3}).

This apparent mismatch between CC and simulation masses is not that severe, for several reasons. First, clump masses are cut at least in $\sim$ half by binary formation, potentially more if mass is lost during collapse [3]. Second, a colder disk is possible, if not very significantly (see below). Third and most important, our choice of $\tilde{G}$ has not been tuned to produce the Kuiper belt, due to the high cost of simulations, and in general is subject to considerable uncertainty. It is feasible that $\tilde{G}$ in the Kuiper belt was significantly lower and thus produced lower mass planetesimals [54], but with a similar shape of the mass distribution [38]. Thus we are confident that our predictions for binary planetesimal properties will not vary significantly if parameters are changed to more closely match CC masses.

4. Pressure gradient

The pressure support parameter $\Pi = nh/2$, where n is the powerlaw exponent $P \propto r^{-n}$ of the gas pressure. Thus simulations with a fixed Π correspond to

$$n = 3/2 + p + q/2 = 2\Pi/h \simeq 1.5 \frac{\Pi}{0.05} \frac{1}{\sqrt{T_{25} R_{45}}} \tag{4}$$

in terms of the exponents $\Sigma_{\rm g} \propto r^{-p}$ and $T \propto r^{-q}$. Thus our nominal parameters correspond to $p + q/2 \simeq 0$ (e.g. a flat $\Sigma_{\rm g}$ and T profile, or one rising and the other falling) which is not consistent with standard smooth disk models. However a standard $p = 3/2, q = 1/2$ model would require an unrealistically cold, $T(45\,{\rm AU}) \simeq 5K$, disk.

We offer two complementary justifications for our choice of a "small" Π value. First, similar to the above discussion of $\tilde{G}$, higher Π values do not have a significant effect on the properties of planetesimals [42]. However, with larger Π, a higher Z value is required to trigger strong SI clumping [10,11,55].

Our second explanation is that a non-standard disk model, with smaller Π, is perhaps a natural explanation of the CC belt. As the outermost planetesimal belt known to form in the solar system, it likely required special conditions. A surface density bump in the disk (which includes a region with $p < 0$) could provide such a condition. Various mechanisms to produce such bumps have been proposed and disk observations find such structures [56]. Note that our proposal is more modest than the production of a particle trap at a pressure maximum (which is also possible).

5. Kozai dynamics and tides

Additional effects that can alter the distribution of newly-formed binaries, and may therefore influence the comparison with observations, include Kozai dynamics and tides [57,58]. The Kozai dynamics of a binary orbit arises due to the gravitational potential of the Sun. For the Kozai cycles to be effective, the two binary components must be roughly spherical and/or the binary separation must be large. If not, the gravitational potential from the J_2 term of the binary components will prevail over the solar gravity, resulting in a simple precession of the binary orbit pole about the heliocentric orbit pole. Ref. [58] studied these effects, including the tidal dissipation [59], and concluded that the combined effect of the Kozai cycles and tides can remove binaries with $i_{\rm b} \sim 90°$ and $a_{\rm b} > a_{\rm crit}$, where $a_{\rm crit}$ depends on J_2 and the strength of tidal dissipation. Given that several observed binaries with $a_{\rm b} < 0.1\ R_{\rm Hill}$ have $i_{\rm b} \sim 90°$, this implies $a_{\rm crit} > 0.1\ R_{\rm Hill}$. Conveniently, most trans-Neptunian binaries have $a_{\rm b} < 0.1\ R_{\rm Hill}$ and their overall inclination distribution was not influenced by these effects. In the main text, we only consider the CC binaries with $a_\mathrm{b} < 0.1\ R_\mathrm{Hill}$ from ref. [6].

6. Caption of the supplementary video

The streaming instability simulation where dense particle filaments form, fragment and gravitationally collapse into planetesimals. The color code shows the integrated column density of particles in the A12 run (density increases from dark blue to light green). The movie starts at time $t = 36/\Omega$, when the particle self-gravity is switched on, and stops at $t = 48/\Omega$, when most particles are bound in clumps. Initially, the streaming instability acts to produce azimuthal filament structures. When the particle self-gravity is switched on, the filaments fragment into chains of gravitationally-bound clumps. The clumps must collapse into planetesimals but the current simulations do not have the capability to follow the collapse stage into completion (i.e., below lengths $\sim$0.1 of the Hill radius). Also, particle collisions are not accounted for in the simulation. The interaction of clumps during the late stages ($t > 42/\Omega$), including tidal disruptions and mergers, is therefore somewhat unphysical.

Supplementary references

[50] Grundy, W. M., Noll, K. S., Nimmo, F., Roe, H. G., Buie, M. W., Porter, S. B., Benecchi, S. D., Stephens, D. C., Levison, H. F., Stansberry, J. A. Five new and three improved mutual orbits of transneptunian binaries. *Icarus* **213**, 678-692 (2011).

[51] Chiang, E., Youdin, A. N. Forming Planetesimals in Solar and Extrasolar Nebulae. *AREPS* **38**, 493-522 (2010).

[52] Natta, A. The temperature profile of T Tauri disks. *Astrophys. J.* **412**, 761-770 (1993).

[53] Whitney, B. A., Robitaille, T. P., Bjorkman, J. E., Dong, R., Wolff, M. J., Wood, K., Honor, J. Three-dimensional Radiation Transfer in Young Stellar Objects. *Astrophys. J. Sup. Series* **207**, 30 (2013).

[54] Johansen, A., Youdin, A. N., Lithwick, Y. Adding particle collisions to the formation of asteroids and Kuiper belt objects via streaming instabilities. *Astron. Astrophys.* **537**, A125 (2012).

[55] Sekiya, M., Onishi, I. K. Two Key Parameters Controlling Particle Clumping Caused by Streaming Instability in the Dead-zone Dust Layer of a Protoplanetary Disk. *Astrophys. J.* **860**, 140 (2018).

[56] Pinilla, P., Youdin, A. Particle Trapping in Protoplanetary Disks: Models vs. Observations. *Astrophys. Space Sci. Lib.* **445**, 91 (2017).

[57] Kozai, Y. Secular perturbations of asteroids with high inclination and eccentricity. *Astron. J.* **67**, 591 (1962).

[58] Porter, S. B., Grundy, W. M. KCTF evolution of trans-neptunian binaries: Connecting formation to observation. *Icarus* **220**, 947-957 (2012).

[59] Goldreich, P., Sari, R. Tidal Evolution of Rubble Piles. *Astrophys. J.* **691**, 54-60 (2009).

[60] Elliot, J. L., and 10 colleagues. The Deep Ecliptic Survey: A Search for Kuiper Belt Objects and Centaurs. II. Dynamical Classification, the Kuiper Belt Plane, and the Core Population. *Astron. J.* **129**, 1117-1162 (2005).

[61] Brown, M. E., Schaller, E. L. The Mass of Dwarf Planet Eris. *Science* **316**, 1585 (2007).

[62] Grundy, W. M., Noll, K. S., Buie, M. W., Benecchi, S. D., Stephens, D. C., Levison, H. F. Mutual orbits and masses of six transneptunian binaries. *Icarus* **200**, 627-635 (2009).

[63] Grundy, W. M., Benecchi, S. D., Porter, S. B., Noll, K. S. The orbit of transneptunian binary Manwë and Thorondor and their upcoming mutual events. *Icarus* **237**, 1-8 (2014).

[64] Grundy, W. M., Porter, S. B., Benecchi, S. D., Roe, H. G., Noll, K. S., Trujillo, C. A., Thirouin, A., Stansberry, J. A., Barker, E., Levison, H. F. The mutual orbit, mass, and density of the large transneptunian binary system Varda and Ilmarë. *Icarus* **257**, 130-138 (2015).

[65] Grundy, W. M., Noll, K. S., Buie, M. W., Benecchi, S. D., Ragozzine, D., Roe, H. G. The mutual orbit, mass, and density of transneptunian binary 229762 2007 UK126, *Icarus*, in press (DOI:10.1016/j.icarus.2018.12.037) (2019b).

[66] Parker, A. H., Kavelaars, J. J., Petit, J.-M., Jones, L., Gladman, B., Parker, J. Characterization of Seven Ultra-wide Trans-Neptunian Binaries. *Astrophys. J.* **743**, 1 (2011).

[67] Sheppard, S. S., Ragozzine, D., Trujillo, C. 2007 TY430: A Cold Classical Kuiper Belt Type Binary in the Plutino Population. *Astron. J.* **143**, 58 (2012).

Object	Dynamical class[a]	$P_{\rm b}$ days	$a_{\rm b}$ km	$e_{\rm b}$	$i_{\rm b}$[b] deg	$M_{\rm tot}$ 10^{18} kg	$a_{\rm b}/r_{\rm Hill}$[c]
26308 1998 SM165	2:1	130.154	11374	0.4732	75.46	6.88	0.02425
42355 Typhon	Centaur	18.9815	1580	0.507	54	0.87	0.0115
50000 Quaoar	Classical	12.431	13330	0.021	-	1210	0.00364
55637 2002 UX25	Scattered	8.309	4750	0.18	65.0	123	0.00314
58534 Logos	Classical	309.9	8220	0.546	74.2	0.458	0.0326
60458 2000 CM114	Scattered	24.825	2500	0.03	56	2.00	0.00667
65489 Ceto	Centaur	9.560	1850	0.008	-	5.5	0.0071
66652 Borasisi	Classical	46.289	4530	0.470	49.4	3.44	0.00916
79360 Sila-Nunam	Classical	12.51006	2770	0.026	123.3	10.8	0.00351
88611 Teharonhiawako	Classical	828.8	27600	0.249	127.6	2.44	0.0581
90482 Orcus	3:2	9.53915	9000	0.0009	106.7	635	0.004311
119979 2002 WC19	2:1	8.403	4090	0.20	-	77	0.00329
120347 Salacia	Scattered	5.49388	5720	0.010	41.4	492	0.00233
123509 2000 WK183	Classical	30.913	2370	0.014	-	1.10	0.00655
134860 2000 OJ67	Classical	22.0585	2270	0.012	-	1.90	0.00523
136199 Eris	Scattered	15.78590	37270	0.0062	78.5	16470	0.004724
148780 Altjira	Classical	139.56	9900	0.344	25.4	3.95	0.0182
160091 2000 OL67	Classical	347.1	7800	0.24	-	0.32	0.035
160256 2002 PD149	Classical	1675	26800	0.588	21.9	0.54	0.099
174567 Varda	Scattered	5.7506	4810	0.022	-	266	0.00232
229762 G!kún‖'hòmdímà	Scattered	11.3147	6040	0.024	32.3	136	0.00383
275809 2001 QY297	Classical	138.118	9960	0.418	161.0	4.10	0.01855
341520 Mors-Somnus	3:2	972.2	20990	0.1494	24.3	0.776	0.0955
364171 2996 JZ81	Classical	1500	33000	0.85	11	1.3	0.090
385446 Manwë	7:4	110.18	6670	0.563	49.1	1.94	0.0167
469514 2003 QA91	Classical	10.1089	1590	0.02	-	3.1	0.00318
469705 2005 EF298	Classical	128.11	7700	0.69	11.2	2.2	0.0178
508788 2000 CQ114	Classical	220.48	6940	0.095	44.4	0.545	0.0253
508869 2002 VT130	Classical	30.761	3030	0.019	-	2.3	0.0067
1998 WW31	Classical	587.3	22620	0.819	51.7	2.66	0.04839
1999 OJ4	Classical	84.115	3310	0.368	57.4	0.405	0.01448
1999 RT214	Classical	126.50	3400	0.30	23	0.19	0.0179
2000 CF105	Classical	3900	34300	0.33	-	0.22	0.166
2000 QL251	2:1	56.449	4990	0.489	134.1	3.09	0.01097
2001 QC298	Scattered	19.2287	3810	0.334	73.7	11.9	0.00502
2001 QW322	Classical	6280	102100	0.464	152.8	2.14	0.223
2001 XR254	Classical	125.58	9310	0.556	21.1	4.06	0.01687
2002 XH91	Classical	371.1	22400	0.71	39	6.5	0.0359
2003 QY90	Classical	309.6	8550	0.663	51.4	0.52	0.0320
2003 TJ58	Classical	137.68	3830	0.516	63	0.236	0.0187
2003 UN284	Classical	3180	54000	0.38	23.0	1.27	0.145
2004 PB108	Scattered	97.020	10400	0.438	83.2	9.5	0.0148
2005 EO304	Classical	3600	69000	0.21	-	2.0	0.155
2006 BR284	Classical	1500	25400	0.275	54.1	0.576	0.0884
2006 CH69	Classical	1420	27000	0.896	133	0.8	0.081

Supplementary Table 1: Properties of trans-Neptunian binaries. Table Notes: **a**. Deep Ecliptic Survey dynamical class [60]. **b**. Inclination of binary orbit, where known. **c**. Semimajor axis in units of Hill radii, a measure of how tightly bound the orbit is. The first uncertain decimal in each figure is the last non-zero decimal shown. Orbital data were published in refs. [6,50,61-67].

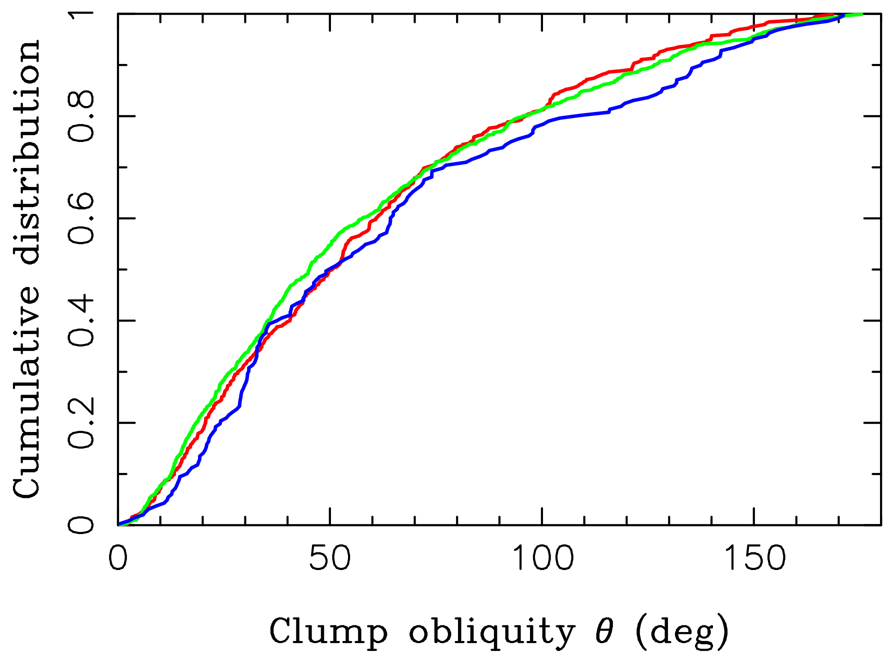

Supplementary Figure 1.— The distributions of clump obliquities in our three SI simulations: A12 (red), B22 (green) and C203 (blue). See Methods for the parameters that were used in these simulations. The obliquity distributions are similar indicating that the general preference for prograde rotation is a defining property of the SI.

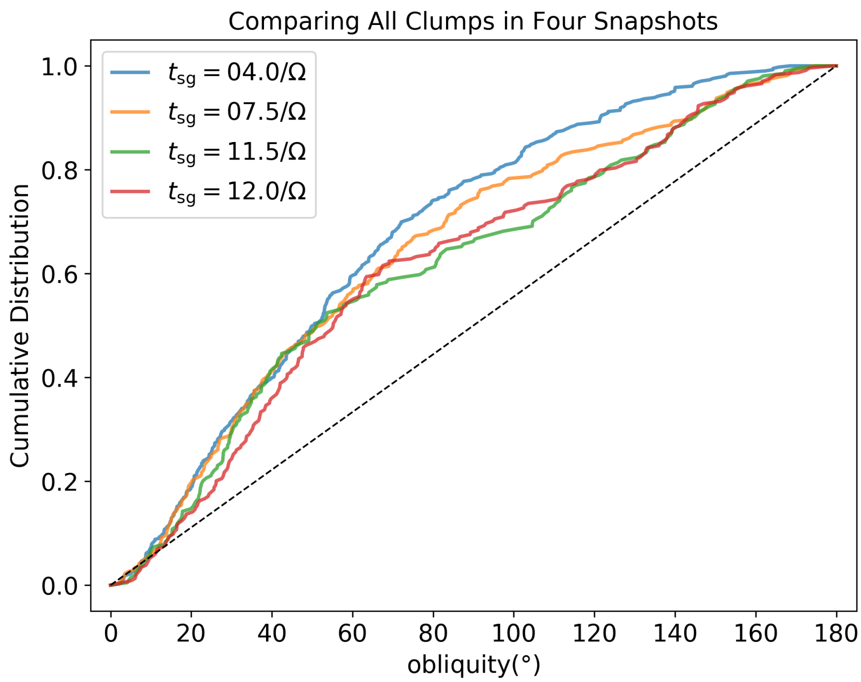

Supplementary Figure 2.— The clump obliquity distributions are shown for four different times in run A12. The particle self-gravity was switched on at $t_0 = 36/\Omega$, where Ω is the Keplerian frequency. Time $t_{\rm sg}$, defined as $t_{\rm sg} = t - t_0$, measures the time elapsed after the particle gravity was switched on.

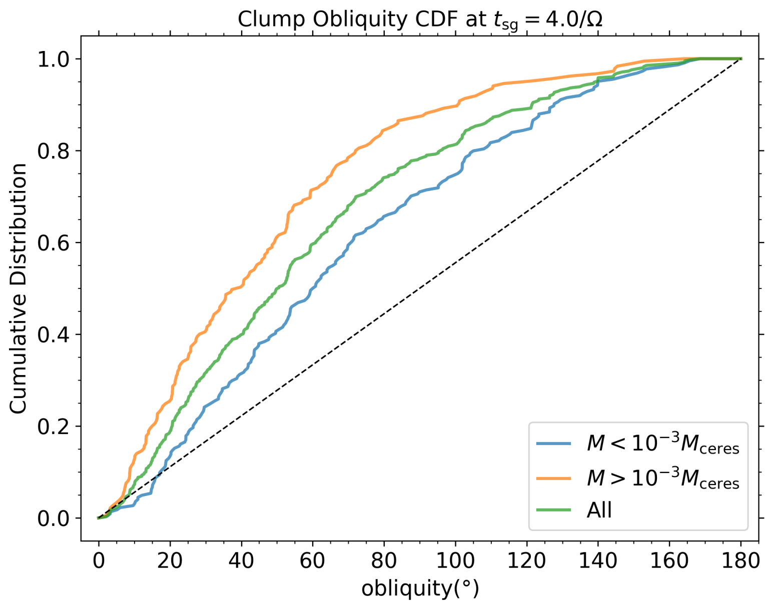

Supplementary Figure 3.— The dependence of the obliquity distribution on clump mass in run A12.

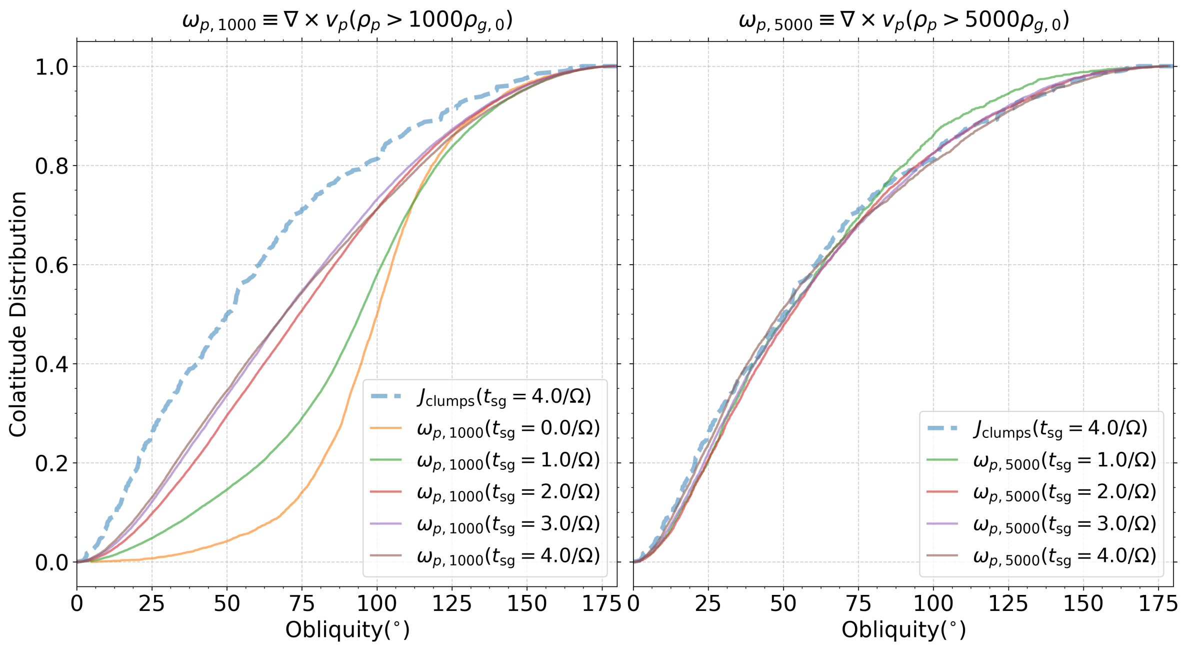

Supplementary Figure 4.— A comparison of the colatitude distribution of the vorticity vectors with clump obliquities for run A12. The colatitude distribution of the vorticity vectors is shown here for cells in which the particle density exceeded a selected threshold. In the left panel and $t_{\rm sg} = 0$, the vorticity vectors show a slight preference for retrograde rotation ($\simeq$60% retrograde vs. $\simeq$40% prograde). In the right panel and $t_{\rm sg} > 0$, the vorticity vectors and clump obliquities both show a strong preference for prograde rotation ($\simeq$80% prograde vs. $\simeq$20% retrograde) .

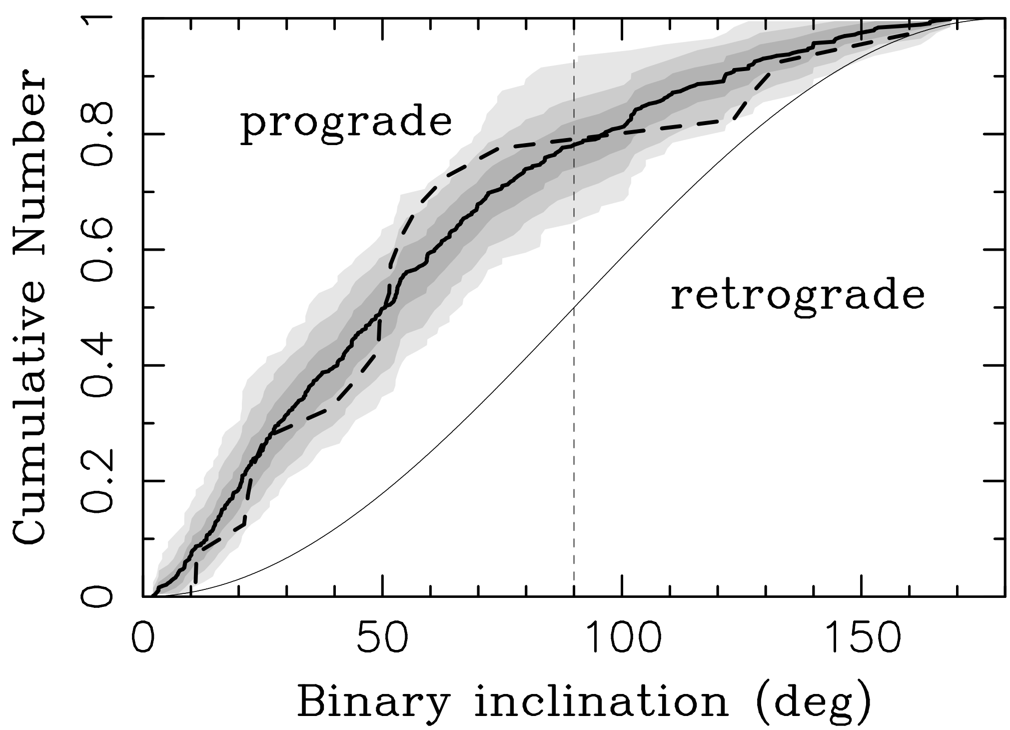

Supplementary Figure 5.— The inclination distribution of binary orbits obtained in the SI model (bold solid line) matches observations of trans-Neptunian binaries (bold dashed line). This figure is the same as Figure 3 in the main text except for the shaded area. Here we draw a sample of 100 model orbits and show three different envelopes with 99.7% (light gray), 95% (medium gray) and 68% (dark gray) model results. The width of the 68% envelope is comparable to the spread of results in different simulations (Supplementary Figure 1). This shows that $\gtrsim$100 binaries will need to be characterized from observations before we could start ruling out some combinations of the SI parameters.